5.3 Surfaces and Interfaces

Highlights of studies of surfaces and interfaces are roughly classified as 1) structures, 2) electronic structures and magnetism, 3) kinetics and dynamics, and 4) applied surface science. We describe them in the following sections.

5-3-1 Structural Studies of Surfaces and Interfaces Using Diffraction

Information on atomic structures of surfaces and interfaces is very important for the understanding of surface properties such as electric and magnetic features, kinetics, and dynamics. Several structures of surfaces and interfaces were determined by *in-situ* X-ray diffraction at BL-15B2. The structure of CH_3S/Au(111) was clarified using photoelectron diffraction at BL-7A.

Interface Reconstructed Structure of Ag/Si(111) -√3 ×√3-Ag

Investigations of metal-semiconductor interfaces have technological importance, because the physical properties of semiconductor devices depend on the characteristics of their interfaces. Horii *et al*. studied a buried interface reconstructed structure of Ag/Si(111)-√3×√3-Ag using grazing incidence X-ray diffraction at BL-15B2 [1]. They found that the interface superstructure can be explained by an inequivalent-triangle (IET) model, as shown in Fig. 1, which has been observed on Si(111)-√3×√3-Ag at low substrate temperatures by STM. The calculated structure factors of the IET model were found to be very close to observed ones. The reliability factor (R-factor) using the IET model was about 25%. The R-factor was improved to be much less value, 12% by considering defects of Ag atoms forming the √3 ×√3 structure.

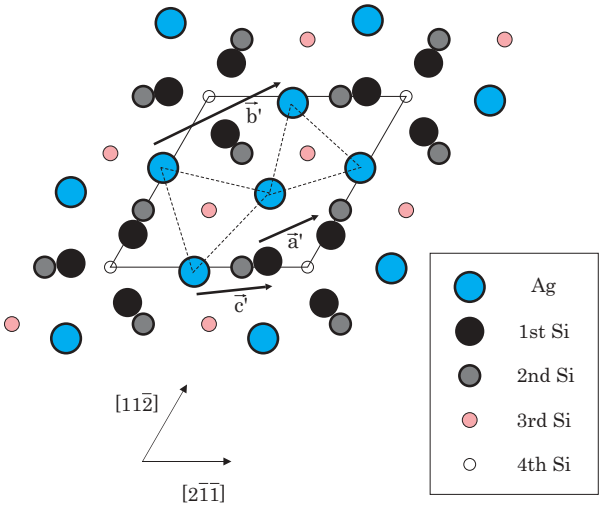

Figure 1
Inequivalent-triangle (IET) model for the Ag/Si(111)-√3×√3-Ag interface structure.

Si(111)-√3×√3-Ag Surface at Room Temperature and Low Temperature

The Si(111)-√3×√3-Ag surface has been attracting interest since its first observation by low-energy electron diffraction in 1967. Its structure had been controversial until a honeycomb-chained triangle (HCT) model was proposed based on surface X-ray diffraction studies in 1988. Recently, however, based on first-principles calculations and scanning tunneling microscopy (STM) experiments at low temperatures, it was suggested that the most stable structure of the Si(111)-√3×√3-Ag surface is not an HCT structure but an inequivalent triangle (IET) structure. Tajiri *et al*. determined in-plane structures of a Si(111)-√3×√3-Ag surface at both room temperature (RT) and 50 K using X-ray diffraction at BL-15B2 [2]. The HCT model with strongly anisotropic thermal vibrations of Ag atoms is preferred over the IET model at RT. On the other hand, at 50 K, the IET model better explains the experimental results. The phase transition temperature of Tc = 150±4 K was obtained from the temperature dependence of the fractional-order reflection intensity. The critical exponent was found to be 0.27±0.03.

Structure and Phase Transition of the Si(113) Surface

Mizuno *et al*. carried out a grazing incidence X-ray diffraction analysis of the Si(113)-3×1 surface at BL-15B2 [3]. They compared the experimental structure factors obtained from the integrated intensities of the fractional-order reflections with calculated ones of the dimerized structure model of Ranke (Fig. 2). By minimizing the R-factor, they determined the position and the size of the pentagon in the 3×1 dimerized structure model of Ranke. In addition, they found that a model with randomly distributed interstitial atoms at the center of the pentagon gives a smaller R-factor value. This result supports an ordering-disordering mechanism for the 3×1 ↔ 3×2 phase transition on the Si(113) surface.

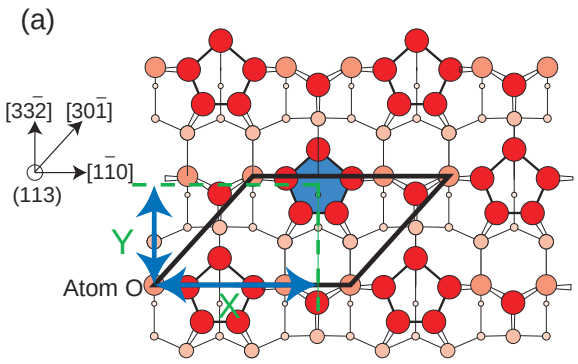

Figure 2
A schematic illustration of the 3×1 dimerized structure model of Ranke. Solid lines indicate the 3×1 unit cell.

Si(111)-6×1-Ag Surface Structure Investigated by X-ray Crystal Truncation Rod Scattering

Sumitani *et al*. analyzed the perpendicular structure of the Si(111)-6×1-Ag surface using X-ray crystal truncation rod scattering at BL-15B2. Least-squares fitting analyses were used for the determination of the atomic arrangement perpendicular to the surface. As a result, the best-fitted model shown in Fig. 3 was obtained. In this model four Si atoms lie on a single layer between the surface Ag layer and the substrate. The heights of the Ag and Si atoms are 3.04 ± 0.01 Å and 2.31 ± 0.01 Å. The R-factor was 0.094.

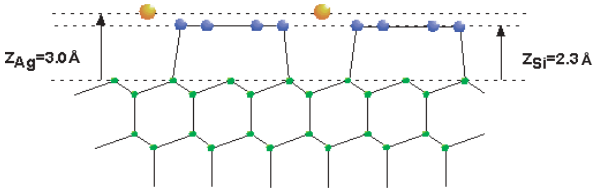

Figure 3
Side view of the Si(111)-6×1-Ag surface structure determined by the fitting procedure.

Structure of Methylthiolate Adsorbed on Au(111) Studied Using Photoelectron Diffraction

Kondoh *et al*. unambiguously determined the structure of methylthiolate (CH_3S) adsorbed on Au(111), a long-standing controversial issue, using scanned-energy and scanned-angle S 2p photoelectron diffraction performed at BL-7A [4]. The methylthiolate molecules were found to occupy atop sites with a S-Au distance of 2.42±0.03 Å. The angular distribution of the S 2p photoelectrons due to forward scattering reveals that the S-C bond is inclined by approximately 50° from the surface normal towards both the [-2 1 1] and [-1 2 -1] (nearest-neighbor thiolate) directions, as shown in Fig. 4.

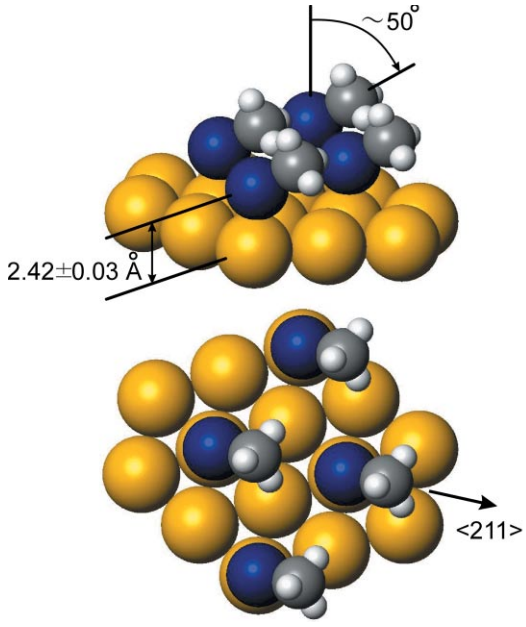

Figure 4
Schematic side and top view of the best-fit adsorption geometry of methylthiolate (CH_3S) adsorbed on Au(111). The hydrogen atoms are shown at tentatively assumed positions.

5-3-2 Electronic Structures and Magnetism of Surfaces

Fermi surface nesting, near surface electronic structure of Cr(001), and the chemical states of the room temperature ferromagnet $ZnGeP_2$:Mn were investigated using photoelectron spectroscopy at BL-7B, BL-3B, and BL-18A, respectively. Metal-induced gap states were studied using near edge X-ray absorption fine structure (NEXAFS) spectroscopy at BL-11B.

Fermi Surface Nesting and Structural Transition on a Metal Surface: In /Cu(001)

Nakagawa *et al.* found that the Fermi-surface nesting of the surface-resonance band induces an order –order structural phase transition on the surface of a normal-state metal; In /Cu(001) [5]. At an In coverage of 0.5, the low-temperature (LT) (9√2×2√2)R45° phase transformed reversibly to the high-temperature (HT) (√2 ×√2)R45° (c(2×2)) phase at ~350 K. Scanning tunneling microscopy of the low-temperature, reduced-symmetry phase indicates a strong periodic lattice distortion (PLD). Angle-resolved photoemission of the high-temperature phase measured at BL-7B reveals that the In-derived surface resonance constitutes a square-shaped, quasi-two-dimensional Fermi surface within the projected bulk Cu bands, as shown in Fig. 5. The Fermi surface exhibits one-dimensional nesting upon the transition, which is in agreement with the PLD periodicity.

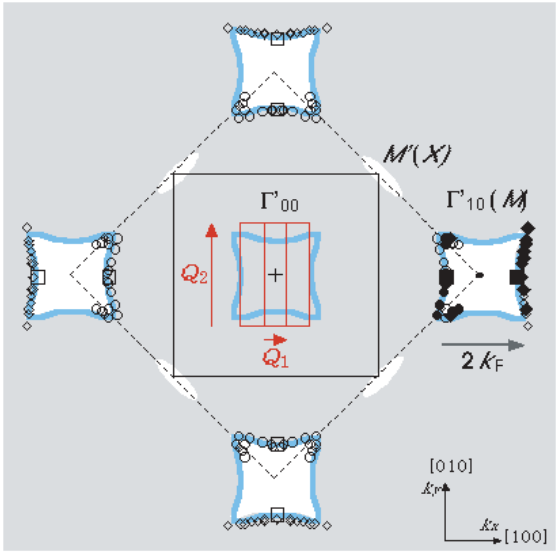

Figure 5
Fermi surface determined for Cu(001)-c(2×2)-In. The solid symbols indicate actual data points. The open ones were generated by mirror operations, and the gray lines indicate that deduced based on the c(2×2) translational symmetry.

An Angle-Resolved Photoemission Study of the Near Surface Electronic Structure of Cr(001)

Nakajima *et al*. measured normal-emission photoelectron spectra of a clean Cr(001) at room temperature with photon energies from 24 to 70 eV at BL-3B [6]. The periodicity of the energy-band dispersion along [001] direction normal to the surface is compatible with that of an antiferromagnetic structure rather than a paramagnetic one. One of the two peaks just below the Fermi level shows energy dispersion, as shown in Fig. 6, which reveals the generally accepted simple picture that these peaks are exchange-split surface states is no longer valid, though the appearance of surface ferromagnetism of Cr(001) is still undeniable.

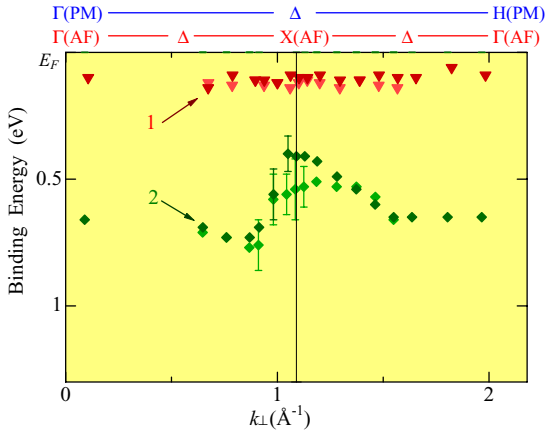

Figure 6
Experimentally observed band dispersion along the Δ-symmetry line. The two points for $h\nu$ = 70 eV are folded back to the left hand side of the figure.

An *In-situ* Photoemission Study of the Room Temperature Ferromagnet $ZnGeP_2$:Mn

Ishida *et al*. studied the chemical states of the $ZnGeP_2$:Mn interface which shows ferromagnetism above room temperature using photoemission spectroscopy at BL-18A, as shown in Fig. 7 [7]. Mn deposition on the $ZnGeP_2$ substrate heated to 400 °C induced Mn substitution for Zn and then the formation of metallic Mn-Ge-P compounds. Depth profile studies showed that Mn 3d electrons changed their character from itinerant to localized along the depth, and in the deep region, dilute divalent Mn species (<5% Mn) was observed with a coexisting metallic Fermi edge of non-Mn 3d character. Their study suggests that the dilute divalent Mn ions, most likely in the substitutional sites of the cations in $ZnGeP_2$, are responsible for the room-temperature ferromagnetism in $ZnGeP_2$:Mn.

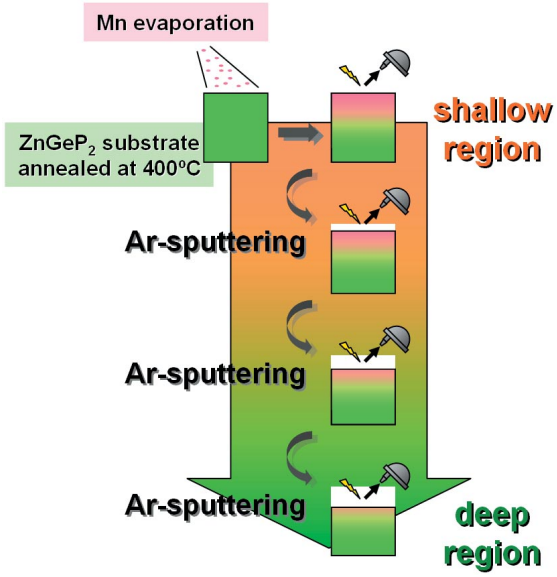

Figure 7
Synthesis and depth profile analysis of $ZnGeP_2$:Mn.

Metal-Induced Gap States at Well Defined Alkali-Halide/Metal Interfaces

In order to search for states specific to insulator/metal interfaces, Kiguchi *et al*. studied epitaxially grown interfaces with element-selective near edge X-ray absorption fine structure (NEXAFS) [8]. An extra peak was observed below the bulk edge onset for LiCl films on Cu and Ag substrates, as shown in Fig. 8. The nature of chemical bonds as probed by X-ray photoemission spectroscopy and Auger electron spectroscopy remained unchanged, so they regarded this as an evidence for metal-induced gap states (MIGS) formed by the proximity to a metal, rather than local bonds at the interface. The dependence on the film thickness showed that the MIGS are as thin as one monolayer. An *ab initio* electronic structure calculation supported the existence of the MIGS that are strongly localized at the interface.

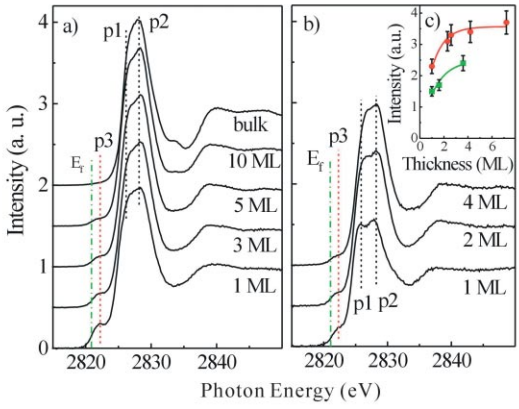

Figure 8
Cl-K edge NEXAFS spectra in LiCl films grown on (a) Cu(001) and (b) Ag(001) for various thicknesses of the LiCl layer. E_f indicates the position of the Fermi level as determined from XPS. Inset (c) shows the intensity of the pre-peak unnormalized versus the film thickness, and the curves are least-squares fits.

5-3-3 Kinetics and Dynamics on Surfaces

Initial oxidation of Si(111) and CO oxidation on oxygen-precovered Pt(111) were investigated using NEXAFS spectroscopy at BL-7A. Spin reorientation transitions of magnetic thin films were studied using XMCD at BL-7A. Novel techniques, energy dispersive NEXAFS spectroscopy and electron polar-angle-resolved-ion coincidence spectroscopy, were developed at BL-7A and BL-8A, respectively.

Initial Oxidation of a Si(111)-7×7 Surface Studied by O K-Edge NEXAFS

Matsui *et al*. investigate the initial oxygen adsorption on the Si(111)-7×7 surface using NEXAFS spectroscopy at BL-7A, as shown in Fig. 9 [9]. Below 220 K, a molecular adsorption species was identified by distinctive absorption resonances due to the $1\pi_g$ molecular orbitals. The molecular species was metastabilized to have a lifetime of 15–35 min at 135 K only with the presence of atomic adsorbates of more than 0.1 monolayer. It was thus clearly evidenced that the very initial adsorption is dissociative even at 100 K and the molecular species is not a precursor state. The molecular adsorption structures with the coadsorbed oxygen atoms were suggested.

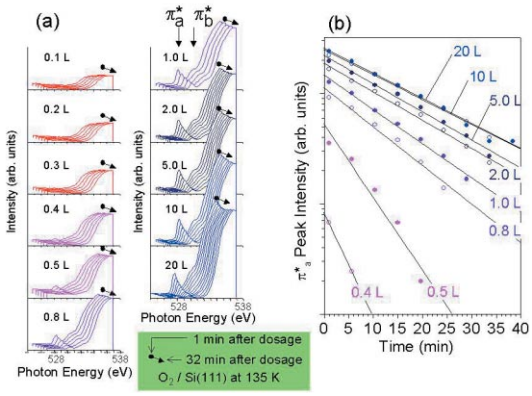

Figure 9
(a) Series of consecutive O K-edge NEXAFS spectra for the Si(111)-7×7 exposed to O_2 at 135 K. (b) Time decay of the π^*_a peak intensities for various O_2 dosages at 135 K.

Study of a Surface Chemical Reaction with Soft X-ray Energy Dispersive Surface NEXAFS

NEXAFS spectroscopy is one of the most suitable to trace the structural and chemical changes during a surface reaction. Amemiya *et al*. successfully developed a novel technique, energy dispersive NEXAFS spectroscopy, by using a position sensitive electron analyzer and a new soft X-ray beamline constructed at BL-7A, as shown in Fig. 10 [10]. It was revealed that the NEXAFS spectra can be obtained even for submonolayer adsorbates with an accumulation period of ~30 sec. Using this technique Nakai *et al*. studied the mechanism of

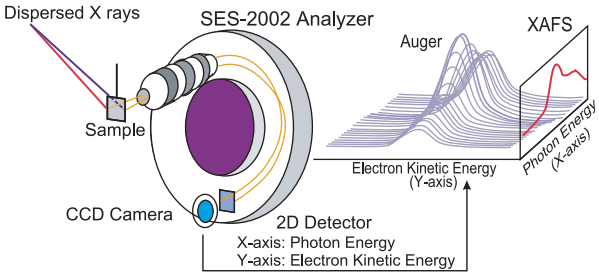

Figure 10
Schematic diagram for the energy dispersive NEXAFS. The horizontal position at the sample surface corresponds to the photon energy.

CO oxidation reaction on oxygen-precovered Pt(111) surfaces [11]. The whole reaction process is composed of two distinct paths: (1) a reaction of isolated oxygen atoms with adsorbed CO, and (2) a reaction of island-periphery oxygen atoms after the CO saturation. CO co-adsorption plays a role to induce the dynamic change in spatial distribution of O atoms, which switches over the two reaction paths. These mechanisms were confirmed by kinetic Monte Carlo simulations.

Spin Reorientation Transitions of Magnetic Thin Films Induced by Chemisorption of Atoms and Molecules

Perpendicular magnetic anisotropy (PMA) is one of the most interesting subjects in magnetic thin films not only from the fundamental aspect of physics but from technological applications. Matsumura *et al*. investigated spin reorientation transitions of ultrathin magnetic films induced by chemisorption of atoms and molecules for CO-, NO-, H- and O-adsorbed Co/Pd(111) and CO- and H-adsorbed Ni/Cu(001) using Co LIII,II- and Ni LIII,II-edge XMCD at BL-7A, as shown in Fig. 11 [12].
A spin reorientation transition from surface parallel to perpendicular magnetization was observed at 200 K after CO dosage. The region of perpendicular magnetic anisotropy (PMA) became about 3 ML thicker at this temperature. For Ni/Cu(001), similar transitions were confirmed when the layers were covered with CO or H, and the PMA range was also expanded, in this case by about 2 ML. The observed stabilization of perpendicular magnetic anisotropy due to chemisorption was ascribed to quenching of the surface parallel magnetic orbital moment.

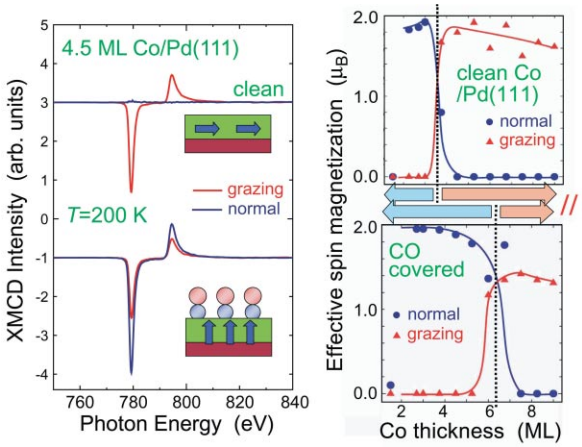

Figure 11
(left) Co L III,II-edge XMCD spectra of 4.5 ML Co/Pd(111) before and after CO adsorption and (right) the spin magnetization of Co/Pd(111) as a function of Co thickness. Remanent magnetization was examined at 200 K.

Development of Electron Polar-Angle-Resolved Ion Coincidence Spectroscopy

In order to investigate mechanisms of ion desorption induced by core-excitations of surface molecules, Kobayashi *et al*. developed apparatus for electron polar-

angle-resolved-ion coincidence spectroscopy at BL-8A, as shown in Fig. 12 [13]. Information on the yield, the mass, the kinetic energy, and the desorption angles of ions can be obtained for the selected Auger final states with this spectroscopy. Using this apparatus, they investigated H^+ desorption induced by a resonant transition from the O 1s level to the $4a_1$ unoccupied orbital ($4a_1 \leftarrow$ O 1s) of condensed water, and confirmed the following four step ion desorption mechanism, that is, (1) $4a_1 \leftarrow$ O 1s transition, (2) extension of the HO-H distance in the $(O\ 1s)^{-1}(4a_1)^1$ state within the lifetime of O 1s hole (ultrafast O-H extension), (3) a spectator Auger transition leading to a state with two valence holes and an excited electron in the $4a_1$ orbital, and (4) H^+ desorption along the potential energy surface of the spectator-Auger final state.

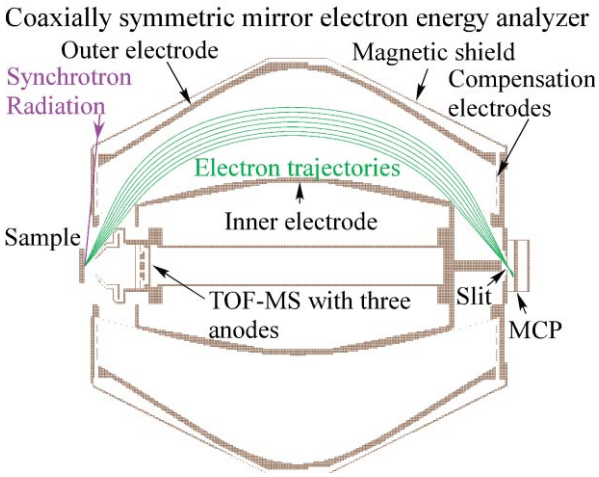

Figure 12.
Electron polar-angle-resolved-ion coincidence analyzer.

5-3-4 Applied Surface Science

Structures of organic materials and LB films were investigated using NEXAFS spectroscopy at BL-11B and BL-7A, respectively. The distribution of ions in the vicinity of a charged surface was studied using XAFS at BL-7C.

Fabrication of a One-dimensional Ordered Structure of α-sexithienyl on Ag(110) and Cu(110)

Organic materials are widely applied for various electronic devices, such as organic electroluminescences and field-effect transistors. Kiguchi *et al*. have studied atomic structures of α-sexithienyl (6T) films grown on Ag(110) and Cu(110) using NEXAFS spectroscopy at the S K-edge at BL-11B [14]. 6T is one of the most promising π-conjugated organic materials. A one-dimensional (1D) ordered structure of 6T with its molecular long axis parallel to the [001] direction could be fabricated, as shown in Fig. 13. Polarization- and azimuth-dependent NEXAFS revealed the formation process of the 1D structure and showed the molecular orientation in the in-plane direction directly. They proposed a new method to obtain the orientation distribution function of molecules using NEXAFS.

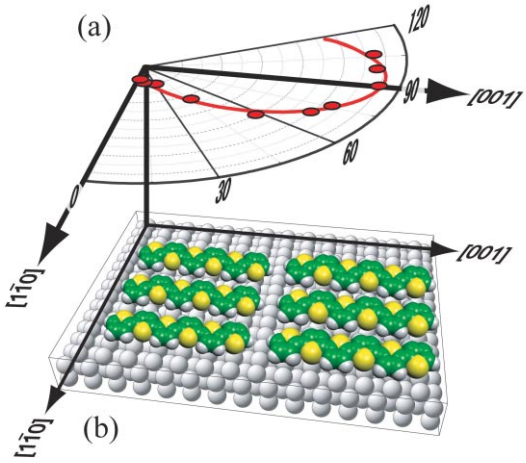

Figure 13.
(a) Polar plot of σ*-peak intensity as a function of azimuth (φ), (b) The schematic model of 1 ML thick 6T on Ag(110).

Change of Molecular Packing and Orientation from Monolayer to Multilayers of Hydrogenated and Fluorinated Carboxylate Studied Using NEXAFS Spectroscopy

Fujimori *et al*. investigated the molecular alignments in LB films of hydrogenated and fluorinated long-chain carboxylates using NEXAFS spectroscopy at the C K-edge at BL-7A. The dependence of C K-edge NEXAFS spectra on the number of layers was studied for cadmium stearate (CdC_{18}) and cadmium perfluorostearate ($CdPFC_{18}$) films. From a Gaussian-function curve-fitting analysis to these spectra at the magic incidence angle ($\theta = 35°$) for the CdC_{18} and $CdPFC_{18}$ 9 layers LB films. For the CdC_{18} films, a change in dependence on the incident X-ray angle between the monolayer and 9–layer samples was clearly found. A similar dependence on the number of layers was not found for the $CdPFC_{18}$ films.

Condensation of Ions at a Surface Monolayer Studied Using XAFS

The knowledge of the distribution of ions in the vicinity of a charged surface plays a key role in explaining electrochemical phenomena, colloid behavior, and ionexchange reactions. Harada and Okada applied total reflection total conversion electron yield X-ray absorption fine structure (TRTCY-XAFS, shown in Fig. 14) to the evaluation of ion exchange occurring at the surface monolayer of didodecyldimethylammonium bromide and dihexadecyldimethylammonium bromide at BL-7C [15]. X-ray absorption measurements at the Br K-edge allow them to detect ion-exchange equilibria between Br- and Cl- added in a subphase. The ion-exchange selectivity of Br- over Cl- basically increases as the monolayer is compressed, indicating that Cl- is selectively squeezed out by compression because of its larger hydrated ionic radius.

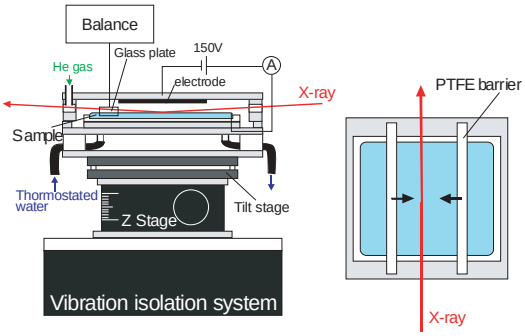

Figure 14.
Schematic view of the TRTCY-XAFS cell.

References

[1] S. Horii, K. Akimoto, S. Ito, T. Emoto, A. Ichimiya, H. Tajiri, W. Yashiro, S. Nakatani, T. Takahashi, H. Sugiyama, X. Zhang and H. Kawata, *Surf. Sci.*, **493** (2001) 194.

[2] H. Tajiri, K. Sumitani, S. Nakatani, A. Nojima, T. Takahashi, K. Akimoto, H. Sugiyama, X. Zhang and H. Kawata, *Phys. Rev. B,* **68** (2003) 035330.

[3] Y. Mizuno, K. Akimoto, T. Aoyama, H. Suzuki, H. Nakahara, A. Ichimiya, K. Sumitani, T. Takahashi, X. Zhang, H. Sugiyama and H. Kawata, *Appl. Surf. Sci.,* **237** (2004) 40.

[4] H. Kondoh, M. Iwasaki, T. Shimada, K. Amemiya, T. Yokoyama, T. Ohta, M. Shimomura and S. Kono, *Phys. Rev. Lett.*, **90** (2003) 066102.

[5] T. Nakagawa, G.I. Boishin, H. Fujioka, H. W. Yeom, I. Matsuda, N. Takagi, M. Nishijima and T. Aruga, *Phys. Rev. Lett.*, **86** (2001) 854.

[6] N. Nakajima, O. Morimoto, H. Kato and Y. Sakisaka, *Phys. Rev. B,* **67** (2003) 041402(R).

[7] Y. Ishida, D.D. Sarma, K. Okazaki, J. Okabayashi, J.I. Hwang, H. Ott, A. Fujimori, G.A. Medvedkin, T. Ishibashi and K. Sato, *Phys. Rev. Lett.*, **91** (2003) 107202.

[8] M. Kiguchi, R. Arita, G. Yoshikawa, Y. Tanida, M. Katayama, K. Saiki, A. Koma and H. Aoki, *Phys. Rev. Lett.*, **90** (2003) 196803.

[9] F. Matsui, H.W. Yeom, K. Amemiya, K. Tono and T. Ohta, *Phys. Rev. Lett.,* **85** (2000) 630.

[10] K. Amemiya, H. Kondoh, A. Nambu, M. Iwasaki, I. Nakai, T. Yokoyama and T. Ohta, *Jpn. J. Appl. Phys.,* **40** (2001) L718.

[11] I. Nakai, H. Kondoh, K. Amemiya, M. Nagasaka, T. Shimada, R. Yokota, A. Nambu and T. Ohta, *J. Chem. Phys*., **122** (2005) 134709.

[12] D. Matsumura, T. Yokoyama, K. Amemiya, S. Kitagawa and T. Ohta, *Phys. Rev. B,* **66** (2002) 024402.

[13] E. Kobayashi, K. Isari, M. Mori, K. Mase, K. Tanaka, K. Okudaira and N. Ueno, *J. Vac. Soc. Jpn.,* **47** (2004) 14 (in Japanese).

[14] M. Kiguchi, S. Entani, K. Saiki and G. Yoshikawa, *Appl. Phys. Lett.*, **84** (2004) 3444.

[15] M. Harada and T. Okada, *Langmuir* **20** (2004) 30.